Analysis of particle rolling and intrinsic rotations in copper powder during sintering

B. Kieback[1] , M. Noethe[1], R. Grupp[1,], J. Banhart[2], T. Rasp[3], T. Kraft[3]

[1]*Inst. of Materials Science, Technische Universität Dresden, Germany.*
[2]*Helmholtz Centre for Materials and Energy Berlin, Germany*
[3]*Fraunhofer Institute for Mechanics of Materials IWM, Freiburg, Germany*

The common theoretical model used to describe the sintering process is the two particle model. This model describes comprehensively the growth of inter-particle contacts driven by the Laplace pressure. In three dimensions this model fails as cooperative material transport (i.e. movements of powder particles) occurs. The fundamental understanding of these processes is still rather sketchy and is derived from the observation of 1D or 2D samples. To observe and quantify cooperative material transport new experimental methods are needed, for example high resolution computer tomography in conjunction with photogrammetric image analysis.

Single crystal copper spheres were marked by drilling holes into the surface of each particle and two samples were prepared using the marked powder. One sample was heated continuously to 1050°C in a silica capillary and was analyzed by in-situ synchrotron computer tomography (SCT) at the ESRF in Grenoble. Free sintering was investigated by ex-situ SCT at Bessy II in Berlin. The novel technique of drilling holes into the sphere surfaces allows for the quantification of both intrinsic rotations and particle rolling by photogrammetry. The observed intrinsic rotations exceed the rolling by far and we conclude that the anisotropy of grain boundary energies results in grain boundary sliding. Furthermore, we present first computer simulations of sintering processes based on initial particle positions measured by SCT.

Keywords: Sintering, fundamentals, focused ion beam, tomography, simulation

Corresponding author: B. Kieback, Bernd.Kieback@ifam-dd.fraunhofer.de,

Tel.: +49 - 351 - 2537 – 300, Fax: +49 - 351 - 2537 - 399

INTRODUCTION

Sintering is utilized to produce thousands of tons of e.g. metallic, hard metal or ceramic components [1-3]. The well understood two particle model is used to describe the fundamental processes occurring in a sintering sample. The minimization of the surface free energy drives the formation and growth of sinter necks by vacancy (and complementary atom) diffusion. This is accompanied by a particle centre approach and causes shrinkage of the sintering component [4-8]. Despite the apparent simplicity of the sintering process several key aspects of the fundamental physics remain elusive. Even model experiments employing 1D arrangements like sphere plate models or particle rows [9-12] or 2D particle arrangements [13, 14] prove the occurrence of movements of entire particles with respect to their contact partners. This phenomenon is called cooperative material transport processes. It classically summarizes translations and rolling of particles. As the entire particle is moved the contribution to the overall shrinkage by rolling of particles into voids of a porous structure can exceed the neck growth mechanisms by several orders of magnitude [15]. Such fast shrinkage by cooperative material transport processes occur predominantly during the initial stages of sintering (heating) [14, 16]. In direct comparison of 2D and 3D samples a significantly higher shrinkage was observed in 2D specimens. This was attributed to the obvious source – the inhibition by higher coordination numbers in 3D samples [14, 16]. Furthermore, the cooperative material transport can have effects beyond a promoted shrinkage such as differential sintering with local densification accompanied by formation of large pores [13, 14, 17]. With rolling we denote the revolution of a particle along the surface of a coordination partner. Cooperative material transport can have a disproportionate impact on sintering behavior as the material volume reassembled by diffusion is minuscule in comparison to the volume of the moved particle. The experiments described in this article add a new cooperative material transport process, the intrinsic rotation. In this work we denote rotation as a motion of a particle around its own centre with little alteration of its contact configuration. Among the driving forces for rolling the anisotropy of grain boundary energies is essential responsible to give rise to rotations [18]. Initially, the particles are statistically oriented. Thus, contact grain boundaries with high excess energies occur frequently. These energies are

accommodated by rolling and rotations. Further driving forces for rolling are stresses inflicted by either asymmetric sinter necks [8, 19] or by inhomogeneities of sintering activities throughout the sintering component [19].

Recent developments enabled the experimental study of cooperative material transport processes beyond 1D and 2D observations. High resolution computer tomography combined with photogrammetric image analysis enabled a quantitative analysis of particle movements. The use of synchrotron computer tomography (SCT) improved the accuracy due to its superior image quality. Further, the brilliance of white beam synchrotron radiation available e.g. at the European Synchrotron Radiation Facility (ESRF) allows for in-situ SCT measurements. First ex-situ (Bernard et. al. [20]) and in-situ (Vagnon et. al. [21] and Lame et. al. [22, 23]) analysis of sintering at the ESRF targeted the investigation of densification, pore distribution, coordination and neck size of glass, copper and steel particles. For the first time it is possible to analyze the particle movements during sintering quantitatively [24, 25]. Currently, we are in an early stage of combining experimental results with computer simulations of the grain boundary energy and simulations of sintering itself.

In this work, we analyze the rotations and rolling of the spherical powder particles in 3D specimens during sintering by in-situ and ex-situ SCT based on experiments described in Ref. 25. Image analysis allows to track all particle positions and all inter particle contacts with high accuracy during the entire sintering process. From this data the rolling angles are easily and quantitatively extracted. The measurement of intrinsic rotations requires additional effort. By using a focused ion beam (FIB) small holes are drilled into the surface of each particle to create markers. An image analysis of the evolution of the positions allows for a calculation of rotation angles from these marker holes. To ensure that the anisotropy of the grain boundary energy is the dominant and clearly defined driving force of both rolling and rotations ideal monocrystalline spheres with diameters of 160 to 200 µm were used [25]. Accompanying to the experiments reviewed in this article, Discrete Element Method simulations of sintering are presented that were adapted to data gained from microtomography experiments focusing on the measurement of rotation and rolling angles. Moreover, a procedure for the calculation of grain boundary energies relating to contact grain boundary misorientations is introduced.

EXPERIMENTS

Monocrystalline powder was produced by the Sauerwald process [26]. Small amounts of copper oxide powder are embedded in alumina powder. Heating copper in a reducing atmosphere up to a temperature beyond the melting point causes the formation of copper droplets, which form nearly perfect copper balls with very few crystallites if the temperature is reduced slowly. For our research these balls can be regarded as monocrystalline balls since the sinter necks will be in all probability in a single crystallite over the entire sintering process and far away from any internal grain boundaries. In the following these particles are considered as monocrystalline. Ideal and non-ideal spheres were separated by rolling the powder over a slightly inclined glass plate.

Two samples consisting of such spheres with a diameter of 160 to 200 µm were prepared. Each of these several hundred monocrystalline balls was marked by one (5*5*8 µm, sample 1) or two (8*8*12 µm, sample 2) holes (Figure 1) by a FIB (ZEISS CrossBeam 1540 EsB).

Sample 1 was analyzed in-situ at the ESRF at Beamline ID15a. In order to measure the particle movements of a loose powder packing in the initial stage (not pre-sintered, starting temperature: 148°C, heating rate: 10 K/min), copper spheres with one marker hole were filled into a silica glass capillary (Ø 1.3 mm) and sintered in a furnace provided by the ESRF. 850 radiograms were acquired in 85 s while the sample was rotated stepwise inside the furnace with X-ray windows by 180°. After 120 s the next tomographic image was acquired. The furnace atmosphere was 96% He mixed with 4% H_2. The resolution of the obtained 3D images was 2.1 µm.

Sample 2 with 2 FIB markers for each particle was measured ex-situ at Bessy II (BAMLine) as the data acquisition time of 6 hours was too long to employ in-situ SCT. This sample was pre-sintered at 650°C for 10 min. After removing the crucible used for pre-sintering the initial state of the samples was measured by SCT. The subsequent sintering stages were prepared by repeatedly heating the sample with 10 K/min to 750°C, 850°C, 950°C and twice to 1050°C in a 90 % N_2 + 10 % H_2 atmosphere. The dwell times at sintering temperature were 10 min

except for the second sintering step at 1050 °C with a dwell time of 1 hour. The resolution obtained at Bessy II was 1.8 µm.

The SCT data sets were analyzed in three steps using custom-made image analysis software. The analysis steps of particle identification, the determination of the accurate particle postion, radius and the identification of the contact partners is described in [24, 25]. The first step of the image analysis is the identification of all particles in the SCT volume. Using a brute force technique a pre-selected sphere volume around each voxel is searched for voxels below a defined threshold. If no value below this threshold can be found the central voxel is defined as possible particle center. This step provides an approximation of particle positions and radii while in the second step the determination of the accurate particle positions and radii is performed. The large particle size implies a small number of particles in the measurement volume. Hence boundary particles were included in the data analysis. Multiple grey value profiles emanating radialy from the approximated centre are analyzed. The maximum derivative of the profile gives the accurate position of the particle surface for the respective direction (artifacts and contact areas are excluded). The refined particle position (accuracy: 0.1 voxels) and radius is then computed by fitting a sphere function to the surface points. Grey value profiles pointing towards a neighboring particle with no significant derivative indicate a sinter neck between the particles, i.e. coordination partners. However the available resolution still prohibits the direct determination of the sinter neck area and particles divided by a small gap of less than 0.5 voxel width cannot be distinguished from contacting particles[1]. The third step of the image analysis is the analysis of the FIB marker hole as described in the supporting online material of [25]. After manually determining the approximated positions of the maker holes, the surface in the vicinity of each marker hole is analyzed with enhanced precision. To provide a high data quality marker holes obscured by image artifacts (for example ring artifacts) are excluded from the data analysis. In sample 1 this leaves 180 and in sample 2 170 particles for analysis. The surface of the sphere is smoothed by a median filter and a spherical shell a few voxel beneath the recalculated surface is transformed within the vicinity of the manually pre-determined marker position into a density map with sub-voxel

[1] The occurrence of such thin gaps is unlikely and metrological inaccessible. Hence must be accepted. The low probability ensures a low statistical significance.

accuracy. The centre of mass of all low density voxels in the map provides the hole position on the particle surface. The 2D positions on the spherical particle surface can be used to calculate the rotations in 3D with an accuracy of 0.1° or better. The accuracy of the derived intrinsic rotation angle (in radians) is the accuracy of the hole position divided by the particle circumference.

An analysis of the resulting data reveals the existence of new and broken sinter necks. A physically meaningful value of rolling is obtained by rotating the coordinate system of one of the two compared sintering stages about a central particle until the sum of angular movements of its coordinating particles is minimized. The average of these angles is assigned to the central particle as its rolling angle. In this rotated coordinate system rolling and rotation of the central particle are separated and rotation angles can be determined by calculating the angular movement of the marker hole. A schematic showing both particle rolling and intrinsic rotations and the consequences for the grain boundary configuration in the contact is shown in Fig 2. Since in sample 1 only one marker per particle was available the rotation data are incomplete. In this case, the calculated rotation is the actually occurring rotation reduced by the cosines between the rotation axis and the axis from particle center to the marker hole. Hence the calculated rotation is in average too low by a factor of $\pi/2$ (assuming a statistical orientation between marker and rotation axis). Calculated rotation angles are always seen as cumulative rotation angles of the previous particle movements, i.e. the angles between the respective stage of sintering and the first measured sintering stage.

EXPERIMENTAL RESULTS

Figure 3 shows a synthesis of maps in sinusoidal projection of the surface of a single crystal copper sphere after pre-sintering and at the end of the sintering process [25]. It shows a contact that was newly formed during the sintering process (1), a broken contact (2), a contact that exhibited no rolling (i.e. the contact kept its position), contacts to particles rolling along the surface of the depicted particle (4) and the marker hole (5). The marker hole shows a much larger and independent change of its angular position than any contact.

Figure 4 shows the average rolling (black dotted line) and rotation (black solid line) angles during in-situ sintering of a copper sample in a silica capillary [25]. In

addition, the figure shows the scatter of average rolling and rotation (solid and dotted grey lines). The final average angle of rotation is approx. 4 °, about twice the final rolling angle. The incomplete rotation data are not yet factored in. With the assumed factor of $\pi/2$ the ratio of rotation and rolling becomes 3.3. Furthermore, the rotations are broken down by the coordination of the rotating particles (colored lines). Both rolling and rotation angle increase continuously during the sintering process and the rotation angles are always significantly higher. It is evident that the rotation declines with growing coordination. The same behavior is found in numerical calculations of the total torque on the particles. Each measured particle contact was assigned a random grain boundary. As simplification it was assumed, that the particular grain boundary only assigns the direction of the torque inflicted on the neighboring particle. The absolute value of torque assigned to each contact was defined as the average torque for grain boundaries with a 110 tilt axis. Specific values of the 110 grain boundary energy were provided by Wolf [27]. The resulting total torque per particle and the torque per contact are shown in Fig. 5 [25].

Figure 6 shows the rotation and rolling angles of sample 2 sintered without silica capillary and analyzed ex-situ at Bessy II [25]. The most significant increase of both rolling and rotation occurs during the first sintering step after pre-sintering. The rotation during this sintering step is approximately 1.2 °. During the subsequent sintering steps only a slight increase up to a value of 1.5 ° can be observed. After the final sintering step (one hour at 1050 °C) an additional increase of the angles is observed and a rotation of about 1.8 ° was measured. The rolling angles are about four times lower than the corresponding rotation angles.

DISCUSSION OF EXPERIMENTS

The particle rearrangements reported in literature are much higher than observed in our experiment [14, 17]. This is due to the analysis of 3D samples, which are subject to more obstructing conditions (in form of a higher coordination number) than the known 2D samples [14, 16]. In literature the process of particle rolling is widely discussed whereas the (intrinsic) rotation is a previously unknown process and hence ignored. Our measurements prove that intrinsic rotations occur. The rotation angles exceed the rolling angles by far and cannot be explained by

existing models. A model of rolling must rely on grain boundary sliding as fundamental mechanism. Except for the anisotropy of the grain boundary energies none of the driving forces of particle rolling can initiate rotations. Further, our samples consist of (almost) ideal spherical particles of the same size. Thus, both inhomogeneous shrinkage and asymmetric sinter necks are not expected. Basically, our samples were designed to exclusively exhibit the impact of the grain boundary energies on both rolling and rotations. With this background the occurrence of high rotation angles can be explained. In 3D samples all particles form a network that obstructs particle rolling. Hence, the grain boundary energies can only be accommodated by intrinsic rotations, which are reflected in their high angle values.

To understand the fact of rotation angles declining with growing coordination we look at both the driving force and the inhibiting forces. The total torque inflicted by the contact grain boundary energies increases monotonic with the coordination. The actually relevant value is the torque per contact as each sinter neck exerts friction as an inhibiting force on rotations. The torque per contact than declines and our samples show the expected behavior.

The observed significant promotion of rolling and rotation in the sample sintered in a silica capillary can be attributed to the differences of the coefficients of thermal expansion of silica and copperWith increase of temperature the silica capillary exerts compressive stress on the sample. These stresses cause particle rearrangements. On top of that the pressure enhances the sintering and, therefore, the higher rate of diffusion enables more pronounced rotations and rolling in sample 1. This is also reflected in a faster growth of coordination in sample 1. Finally, the the most extensive cooperative material transport processes occur in the initial stages of sintering as also observed by some other authors [15, 16].

SIMULATION

In addition to the experimental investigation of particle rotation during sintering, accompanying simulations are performed in order to analyze the influence of different powder parameters like particle size or inter-particle friction that cannot be changed easily in experiment. A particle-based approach is chosen on the basis of the Discrete Element Method (DEM). Each powder particle is defined by its position, radius, velocity and angular velocity and can interact with other adjacent

particles. Assuming that grain boundary diffusion is the main transport mechanism for sintering and that the surface of the pores is in equilibrium (regime of open porosity), the interaction between two neighboring particles is determined so far by the following force laws [28]

$$F^n = \gamma_s(2\mathrm{A}\kappa + L\sin\psi) + \frac{\pi c^4 k_b T}{8\Omega\delta D_b} v_{ij}^n \qquad (1)$$

in normal and

$$F^t = \eta \frac{\pi c^2 R^2 k_b T}{8\Omega\delta D_b} \left(\left(v_{ij} - v_{ij}^n \hat{r}_{ij}\right) + \frac{r_{ij}}{2} \times \left(\omega_i + \omega_j\right) \right) \qquad (2)$$

in tangential direction. Here, k_B is the Boltzmann constant, T the temperature, Ω the atomic volume, δD_b the grain boundary thickness times the grain boundary diffusion coefficient, which has an Arrhenius type temperature dependence, $\delta D_b = D_{b,0} \exp(-Q_{gb}/k_b T)$, where Q_{gb} is the activation energy for grain boundary diffusion. $A = \pi c^2$ is the contact area between particles with radius c, L the length of its perimeter, κ the curvature of the surface, γ_s the specific surface energy and ψ the dihedral angle. The normal distance between the particle centres is denoted by r_{ij}, whereas $\hat{r}_{ij} = r_{ij} / |r_{ij}|$ is the unit vector in the direction perpendicular to the contact area. $v_{ij} = v_i - v_j$ is the relative particle-particle velocity, v_{ij}^n its component in the direction perpendicular to the contact area and ω_i the angular velocity of a particle i. The tangential viscous force can be controlled by a phenomenological dimensionless viscosity parameter η that determines the sliding behaviour of two particles. The normal force F^n leads to an approximation of adjacent particles and – depending on neighboring particles – to particle rearrangements. The particles are subjected to tangential forces primarily triggered by the effect of grain boundary anisotropies being the major mechanism which causes particle rotations. This force is not implemented yet. The other tangential force F^t mentioned above is minor to the one initiated by grain boundary misorientations and is caused by contact friction. It also imposes a small torque to particles inducing slight intrinsic rotations. The calculation of grain boundary energies as a function of contact grain boundary misorientations (which is part of our actual work as shown later) is a crucial step towards the introduction of this effect into the simulation model.

The total force as well as the total torque acting on a particle is calculated from the sum of particle-particle forces and torques. The temporal evolution of the particle system is governed by Newton's equations of motion, where the time integration is performed by the Velocity-Verlet algorithm [29]. Information on the numerical implementation of the propagation scheme and the acting forces can be found in [30].

In order to analyze the particle rotation during simulation, the orientation of each particle, which is assumed to be a single crystal, is initially assigned with a fixed orientation vector φ^{init} that has the same indication function as a FIB hole in reality. The spatial rotation of the marking vector of particle i is propagated in time according to $\dot{\varphi}_i = \omega_i \times \varphi_i$ with a temporal dependence for the angular velocity of $\dot{\omega}_i = \frac{\tau_i}{I_i}$, where τ_i is the torque acting on particle i and I_i its moment of inertia. The rotation angle α_i can then be determined by the relation $\cos\alpha_i = \frac{\varphi^{init}}{\|\varphi^{init}\|} \cdot \frac{\varphi_i}{\|\varphi_i\|}$. For the determination of rolling angles, the linking vectors between the centers of two particles initially being in contact are saved. As long as a contact still exists, an updated linking vector is detected and a comparison with the initial link provides the actual rolling angle between this particle pair. Applying this procedure, free sintering simulations were performed on an initial particle setup that was configured by about 7600 particle positions and radii (figure 7) which correspond to a real particle packing used in an experiment carried out at ESRF . The particle data was gained by analyzing micro tomography images taken during the experiment. The average particle diameter was about 59.9 µm and experimental pre-sintering was performed at 650 °C for 10 min in order to be able to analyze free sintering i.e. without the constraint imposed by a capillary.

The simulation parameters are taken from [31] except of the pre-exponential factor $D_{b,0}$ that is used as a fitting parameter. A heating scheme as displayed in figure 6a is applied to the sample. Figure 8b shows the densification for a value of $D_{b,0} = 9.5\text{x}10^{-13}$ m^3/s. The plot reveals good accordance of experimental measurements and computed results at least for the period of isothermal sintering. The origin of the partial desintering during the heating region observed in the experiments is currently investigated.

Figure 9a shows the temporal development of the average rotation and rolling angles in the simulation for two different friction parameters η. The rotation angles of all particles in the sample were considered for the calculation, whereas about 14.500 particle pairs were taken into account for the averaging of the rolling angle. Even when the effect of rotations due to grain boundary misorientations is still not considered as stated before, it can be seen that the rotation angle exceeds the rolling angle. The ratio between rotation and rolling angle of about 2.5:1, however, is lower than the ratio of 4:1 measured in the related (but not comparable) experiment shown in figure 6, which demonstrates that the effect of anisotropic grain boundaries has a significant contribution to the intrinsic rotation of particles.

Separating the particles into a core group and a border group (consisting of the outer layer of particles) in figure 9b reveals the expected situation of higher rolling and rotation angles for border particles, since their coordination number is lower than those of core particles.

This simulation model must be complemented by the calculation of the energies of grain boundaries as a function of the contact grain boundary misorientations. Currently we are developing a molecular dynamics code that allows for the simulation of arbitrary grain boundary misorientations. The simulation volume on either side of the grain boundary has to be periodic in the plane parallel to the grain boundary. We define these periodic coordinates to be the x and y coordinates, z is the coordinate perpendicular to the grain boundary. It is not necessary that the volume of the combined crystals is periodic. The first step is the calculation of the minimal simulation volumes of both crystals. In case of an asymmetric grain boundary these volumes are not equal and it is necessary to extend the crystal with smaller x dimension by an integral multiple of that dimension, so that the x dimension is at least as big as the x dimension of the other crystal. A similar adjustment of the y dimension is also necessary. This adjusted simulation volumes can be filled with atoms. The periodic coordinates in x and y direction ensures that the crystal can be extended unlimited in x and y direction by virtual atoms (atoms translated by multiples of the x and y dimension). An atom layer both at the top of the upper crystal and at the bottom of the lower crystal with a thickness equal to the range of the potential is fixed and the fixed atoms are used as interaction partners for the non fixed atoms.

The next step is crucial for a successful calculation of the grain boundary energy of a symmetric grain boundary. One of the two crystals is moved to various positions in x and y direction. For each position the z coordinate is adjusted to minimize the energy. After selection of the optimal relative position of both crystals further atoms are added at positions far from the next atom. A small region of the simulation volume (four times the lattice parameter around the grain boundary) is allowed to relax. The atom with maximal energy is removed and the procedure is repeated until a minimum of the grain boundary is found. After this adjustment of the number of atoms (of the atom density of the simulation volume) the entire crystals are relaxed and a final value of the grain boundary energy is computed.

In case of the asymmetrical grain boundaries this procedure is altered because the simulation volume is no longer periodic (each crystal by itself is still periodic). The relaxed crystals are calculated for each y-x raster position and subsequently all grain boundary energies for one misorientation are averaged.

Figure 10 shows the grain boundary energy for various misorientations of symmetrically tilted grain boundaries for a (100) tilt axis. Like the values obtained by Wolf [27] for symmetric grain boundaries for the same tilt axis there are no pronounced minima found for these grain boundaries, i.e. for the (100) tilt axis there are no special grain boundaries. After this "proof of concept" a data base of grain boundary energies is created. This data will be embedded in the DEM simulations of sintering in a future step.

CONCLUSION

The novel technique of analyzing the sintering of 3D particle packings using high resolution SCT employing spheres with marker holes allowed us to observe intrinsic rotations for the first time. Obviously the anisotropy of the grain boundary energies is is the reason for particle rotations against the friction of grain boundary sliding. 1D samples exhibit more extensive rolling movements than 3D samples as the 3D network inhibits particle rearrangements. An analysis of the sintering process with the help of high resolution SCT is an interesting method, but the scientific merit is in a deeper understanding of the sintering process based on this quantitative data. In a first step we use DEM computer

simulations based on the initial state of a specimen analyzed by SCT. The comparison of the simulation results with the SCT measurements of the subsequent sintering stages with respect to densification shows promising similarities. To complete the simulation model torques induced by the grain boundary energies have to be introduced to the simulation model. For this purpose a model to simulate arbitrary grain boundaries is developed. First results are presented in this article.

ACKNOWLEDGEMENTS

The authors would like to thank the Deutsche Forschungsgemeinschaft (DFG) for funding of our research. In addition we would like to thank the Helmholtz Gemeinschaft for funding of the Virtual Institute 'Photon and Neutron Research on Advanced Engineering Materials', H. Riesemeier for the support at the BAMLine and Ecka Granulates for supplying copper powder. We are grateful to the European Synchrotron Radiation Facility for the provision of synchrotron radiation facilities and especially M. Di Michiel for his assistance in using beamline ID15A.

REFERENCES

1. German RM (1996) Sintering theory and practice. John Wiley, New York
2. Schatt W, Wieters K-P and Kieback B (2007) Pulvermetallurgie: Technologien und Werkstoffe. Springer
3. German RM (2005) Powder metallurgy and particulate materials processing. Metal Powder Industries Federation, Princeton
4. Exner HE and Kraft T (1998) Review on computer simulations of sintering processes. (Proc. Powder Metallurgy World Congress, Granada (Spain) 18.-22.10.1998 (European Powder Metallurgy Association, Shrewsbury) 2:278–283
5. Exner HE (1979) Principles of single phase sintering. Rev Powd Met Phys Ceram 1:7-251
6. Schatt W (1992) Sintervorgänge. VDI-Verlag, Düsseldorf
7. Geguzin JE (1973) Physik des Sinterns. VEB Deutscher Verlag für Grundstoffindustrie, Leipzig
8. German RM (1994) Powder Metallurgy Science. 2nd Ed. Metal Powder Industries Federation, Princeton
9. Mykura H (1979) Grain-boundary energy and the rotation and translation of Cu spheres during sintering on a substrate. Acta Metall 27:243–249

10. Wieters K-P, Boiko IJ and Schatt W (1984) The mechanism of the rotation of single-crystal spheres during sintering. Cryst Res Technol 19:1195–1200

11. Pond RC and Smith DA (1977) Relative rotation of unconstrained polycrystals. Scripta Metall 11:77-79

12. Chan SW and Balluffi RW (1986) Study of energy vs. misorientation for grain boundaries in gold by crystallite rotation method - II. Tilt boundaries and mixed boundaries. Acta Metall 34:2191-2199

13. Weiser MW and De Jonghe LC (1986) Rearrangement during sintering in two-dimensional arrays. J Am Ceram Soc 69:822–826

14. Exner HE and Müller C (2009) Particle rearrangement and pore space coarsening during solid-state sintering. J Am Ceram Soc 92:1384–1390

15. Skorokhod VV (1999) Rapid rate sintering of dispersed systems: Theory, processing and problems. Powder Metall and Metal Ceram 38:350-357

16. Eloff PC and Lenel FV (1971) The effects of mechanical constraints upon the early stages of sintering. Modern developments in powder metallurgy, Volume 4; Proceedings of the International Powder Metallurgy Conference, New York, N.Y ; United States; 12-16 July 1970 291-302

17. Petzow G and Exner HE (1976) Particle rearrangement in solid state sintering. Z Metallkde 67:611-618

18. Sutton AP, and Balluffi RW (2003) Interfaces in Crystalline Materials. Oxford University Press

19. Petzow G and Exner HE (1976) Particle rearrangement in solid-state sintering. Z Metallkd 67:611–618

20. Bernard D, Gendron D, Heintz J-M, Bordère S and Etourneau J (2005) First direct 3D visualisation of microstructural evolutions during sintering through X-ray computed microtomography. Acta Mater 53:121–128

21. Vagnon A, et al. (2008) 3D statistical analysis of a copper powder sintering observed in situ by synchrotron microtomography. Acta Mater 56:1084–1093

22. Lame O, Bellet D, Di Michiel M and Bouvard D (2003) In situ microtomography investigation of metal powder compacts during sintering. Nucl Instr Meth Phys Res B 200:287-294

23. Lame O, Bellet D, Di Michiel M and Bouvard D (2004) Bulk observation of metal powder sintering by X-ray synchrotron microtomography. Acta Mater 52:977–984

24. Nöthe M, Schulze M, Grupp R, Kieback B and Haibel A (2007) Investigation of sintering of spherical copper powder by micro focus computed tomography (µCT) and synchrotron tomography. Mater Sci For 539–543:2657–2662

25. Grupp R, Nöthe M, Kieback B and Banhart J (2011) Cooperative material transport during the early stage of sintering. Nat Comm 2:298

26. Sauerwald F and Holub L (1933) Kristallisation zwischen möglichst weitgehend im Strukturgleichgewicht befindlichen Oberflächen (Crystalisation between preferably wide in structure balanced surface tension). Z Elektrochem Angew Phys Chem 39:750–753

27. Wolf D (1990) Correlation between structure, energy and ideal cleavage fracture for symmetrical grain-boundaries in FCC metals. J mater Res 5:1708-1730

28. Riedel H, Zipse H and Svoboda J (1994) Equilibrium pore surfaces, sintering stresses and constitutive equations for the intermediate and late stages of sintering--II. Diffusional densification and creep. Acta Metall 42:445-452

29. Verlet L (1967) Computer 'experiments' on classical fluids. I. Thermodynamical properties of Lennard-Jones molecules. Phys Rev 159:98-103

30. Henrich B, Wonisch A, Kraft T, Moseler M and Riedel H (2007) Simulations of the influence of rearrangement during sintering. Acta Mater 55:753-762

31. Swinkels FB and Ashby MF (1981) A second report on sintering diagrams. Acta Metall 29:259-281

Figure Captions

Fig. 1 Single crystal Cu particle with FIB marker holes

Fig 2 a) Schema of rolling and rotations based on the schema in [25]

Fig 2 b) Schema of the consequences of rotations (left) and rolling (right) for the contact grain bounary

Fig. 3 Synthesis of maps of the surface of a sintering single crystal copper particle at 148 °C and 1082 °C [25]

Fig. 4 Average rolling and rotation angles (including the respective scatterbands) of single crystal copper spheres during sintering in a silica capillary and rotations broken down by coordination [25]

Fig. 5 Simulation of the torque and torque per contact on a sintering particle with respect to the coordination number [25]

Fig.6 Average rolling and rotation angles of single crystal copper spheres during free sintering, measured ex-situ [25]

Fig. 7 Initial configuration for simulation adapted to a real sample

Fig. 8 a) Applied heating scheme

Fig. 8 b) Densification of the cylindric sample

Fig 9 a) Averaged rotation (solid) and rolling angle (dashed) in a free sintering simulation for two friction parameters;

Fig. 9b) Development of averaged rotation (solid) and rolling angle (dashed) in the same simulation split into particles at the border and in the core of the sample for a friction parameter of $\eta = 0.01$.

Fig. 10 Grain boundary energy vs. tilt angle for a 100 tilt axis

Figure 1
Click here to download high resolution image

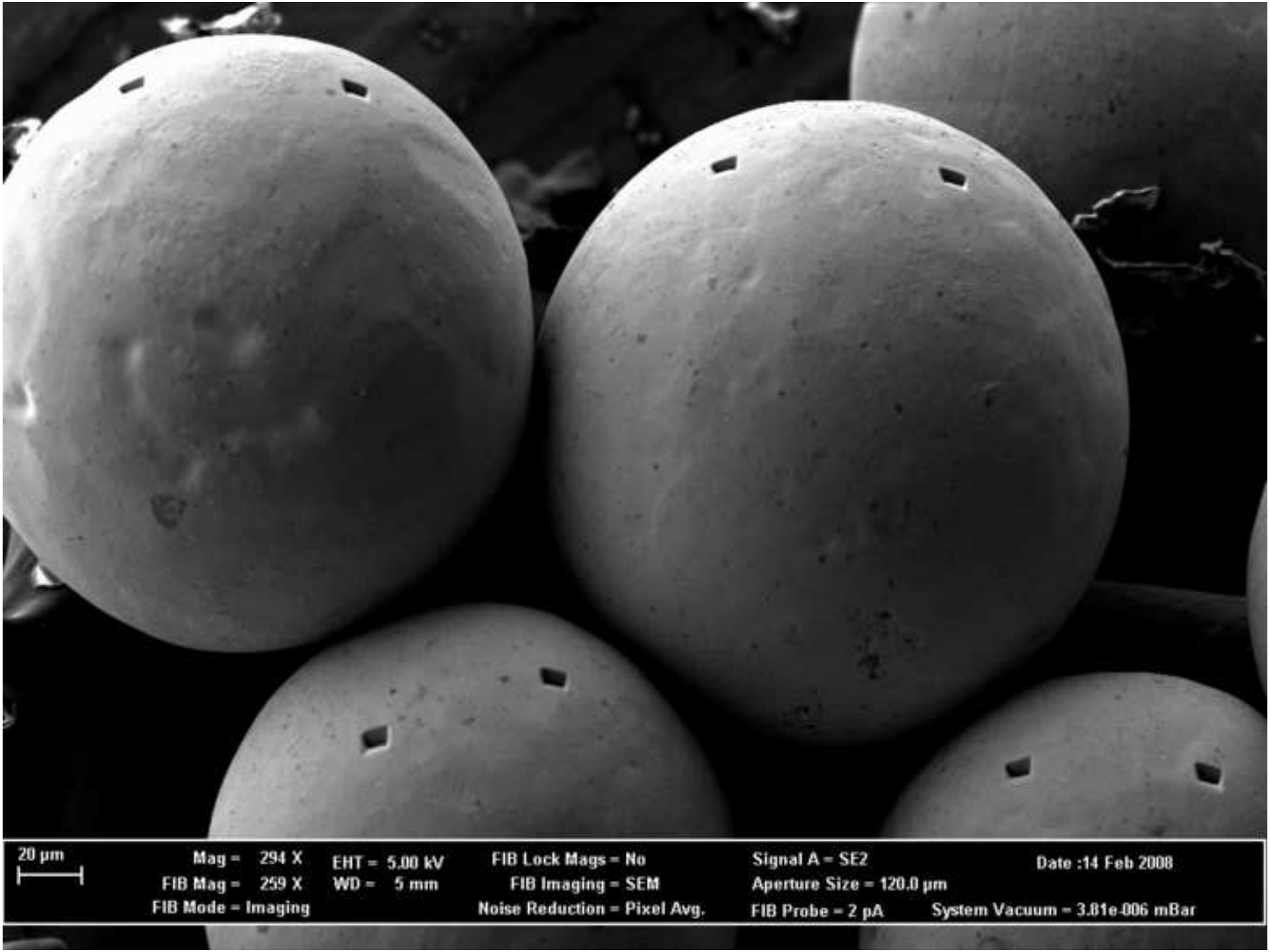

Figure 2a
Click here to download high resolution image

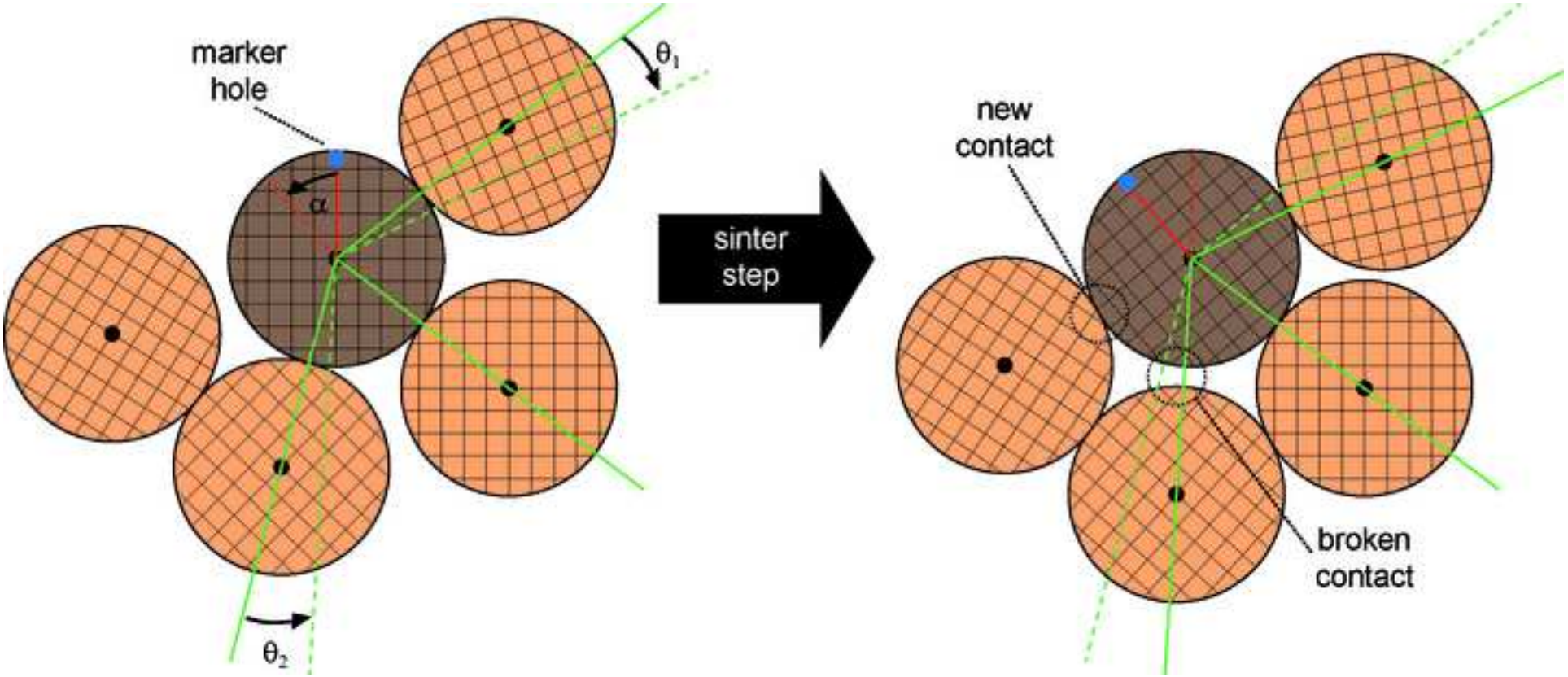

Figure 2b
Click here to download high resolution image

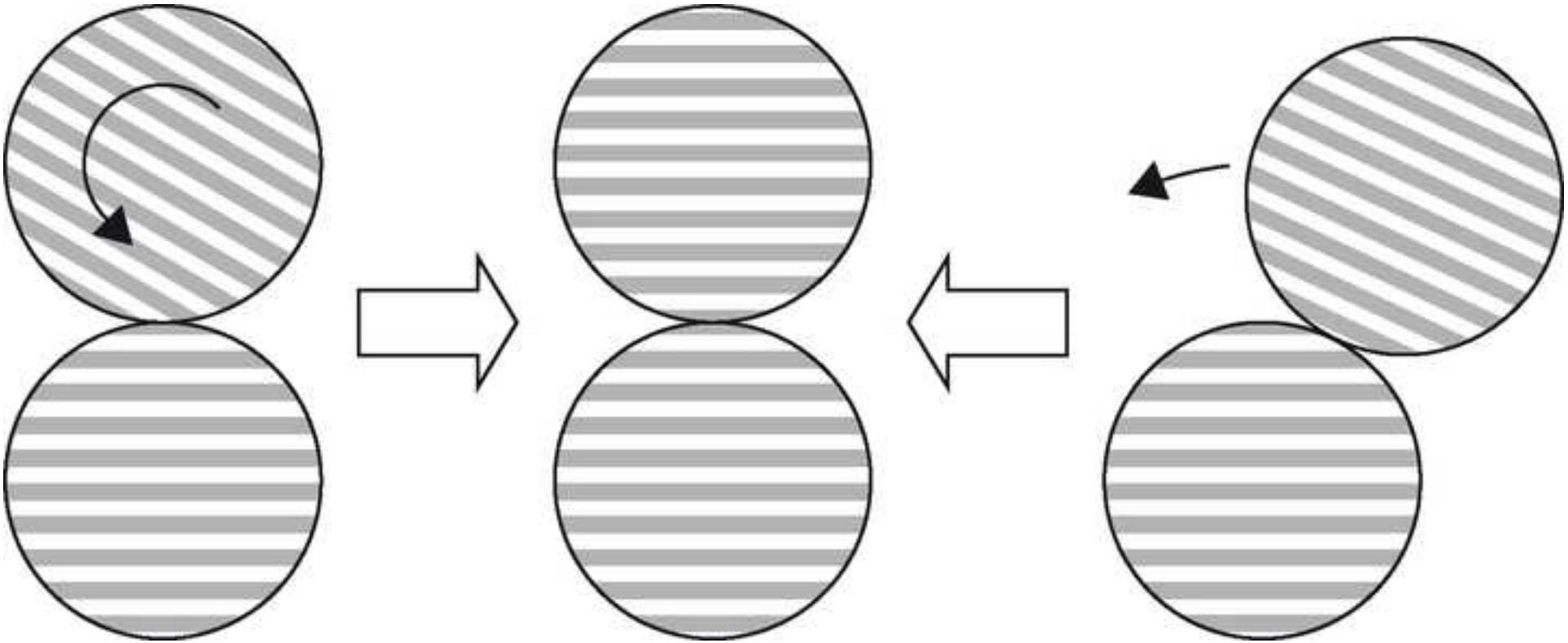

Figure 3
Click here to download high resolution image

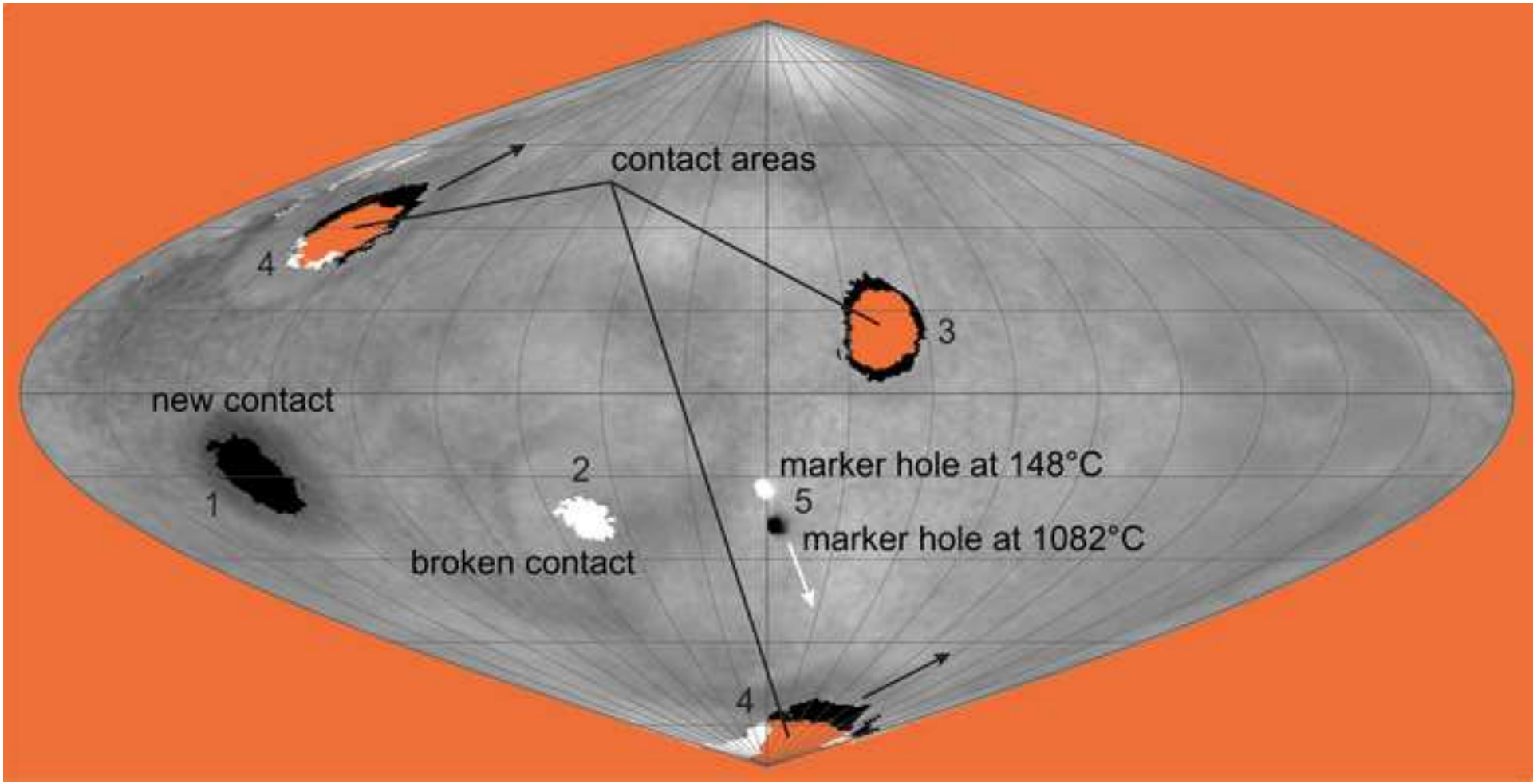

Figure 4
Click here to download high resolution image

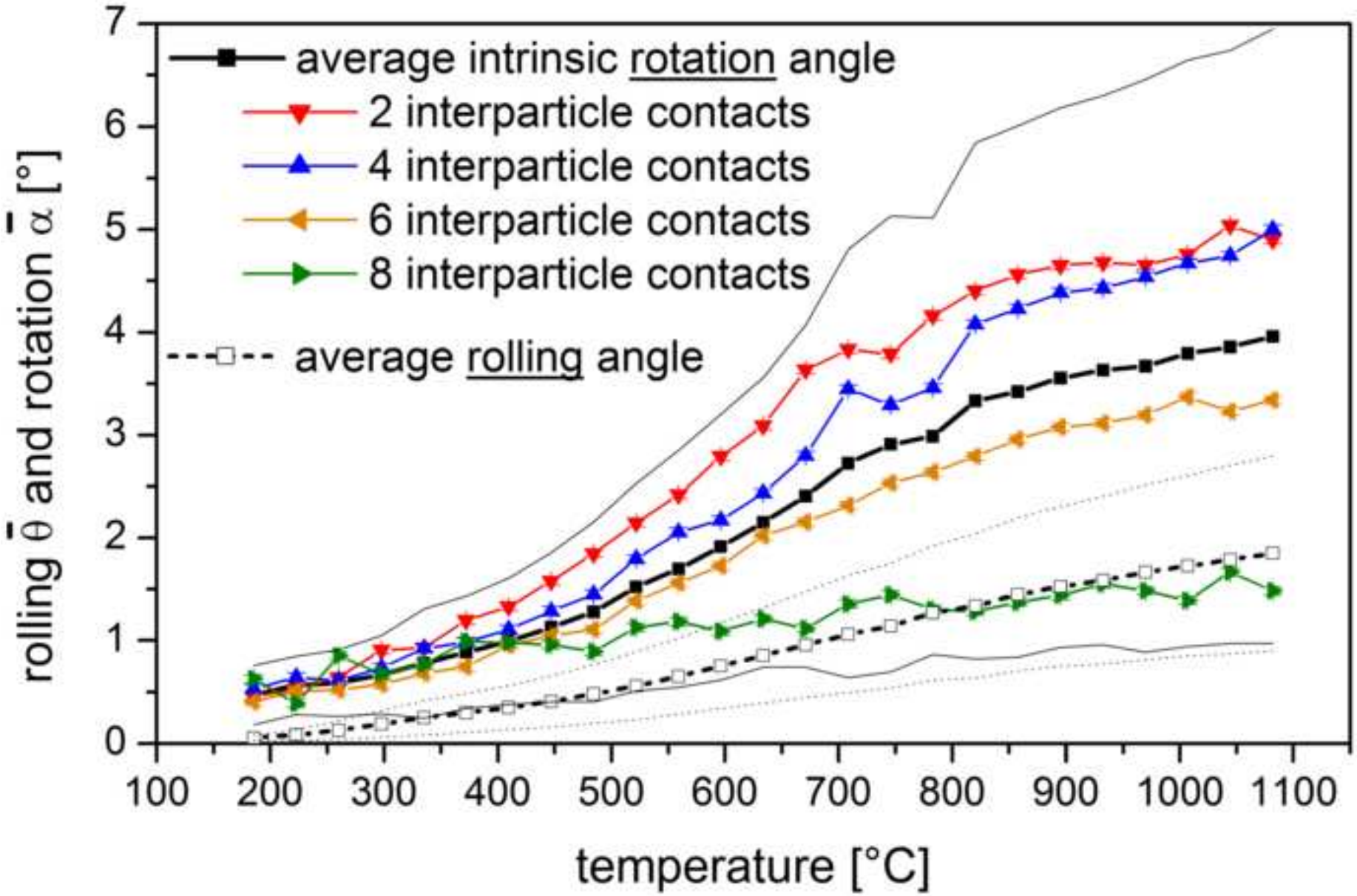

Figure 5
Click here to download high resolution image

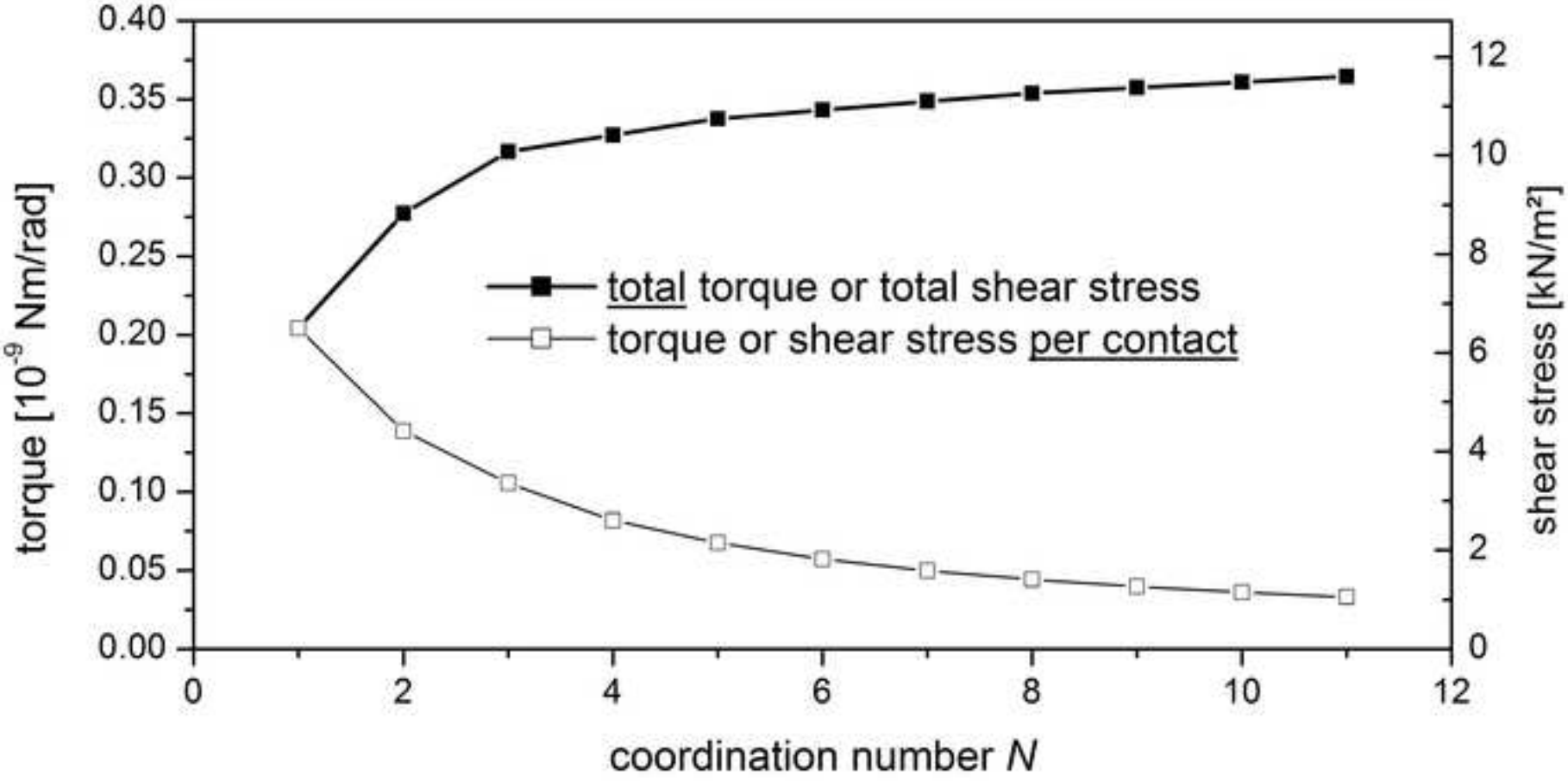

Figure 6
Click here to download high resolution image

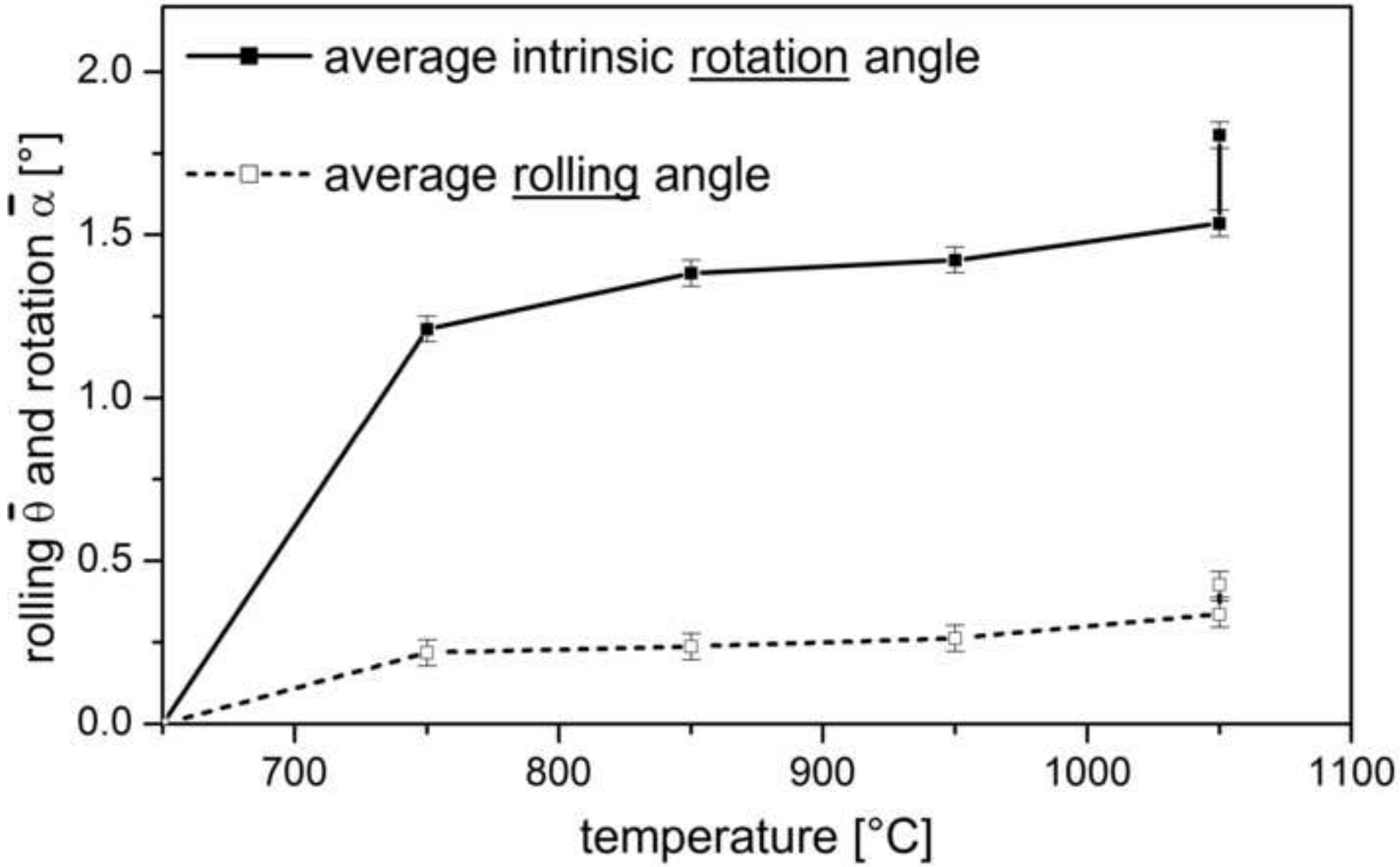

Figure 7
Click here to download high resolution image

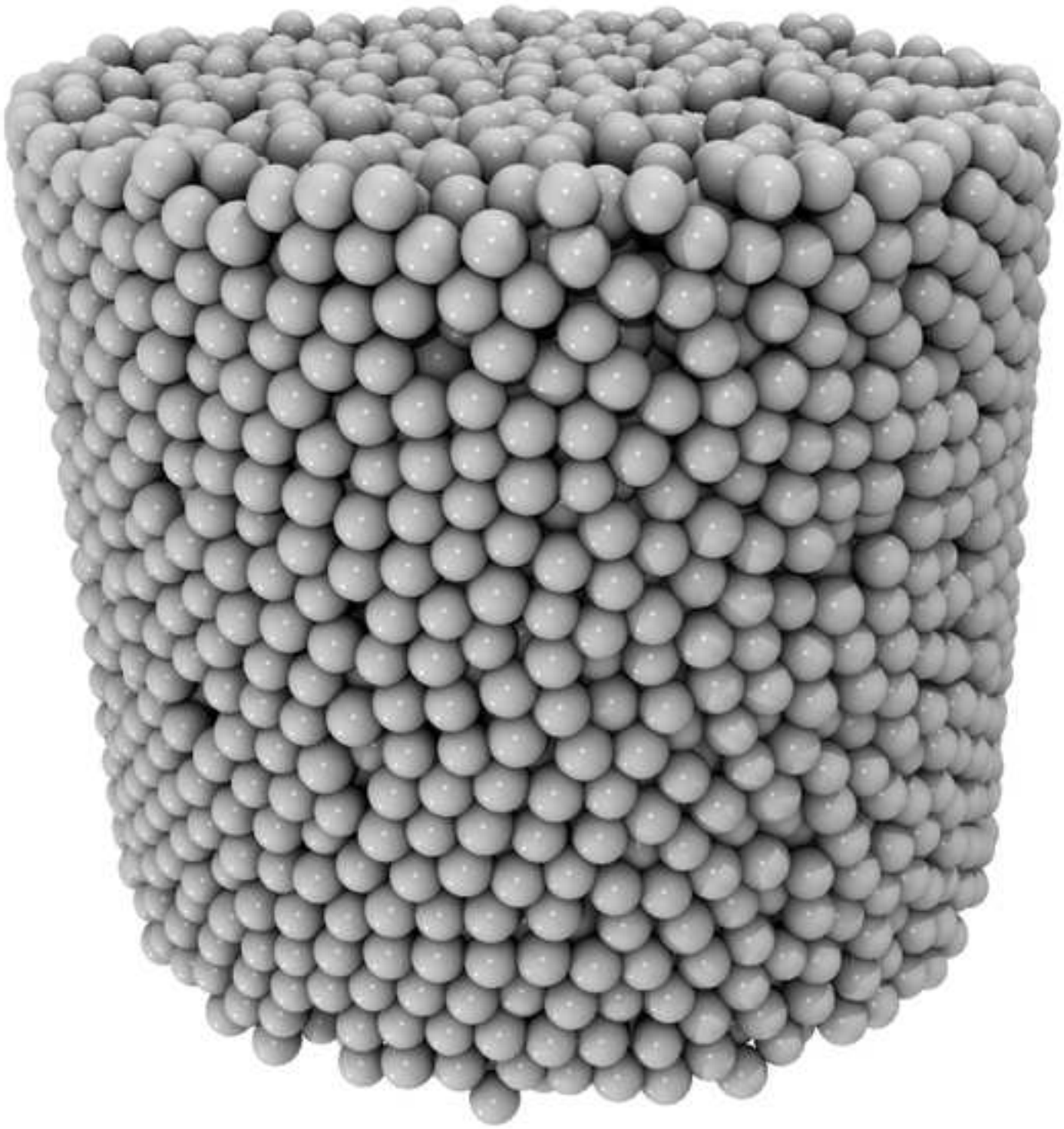

Figure 8a
Click here to download high resolution image

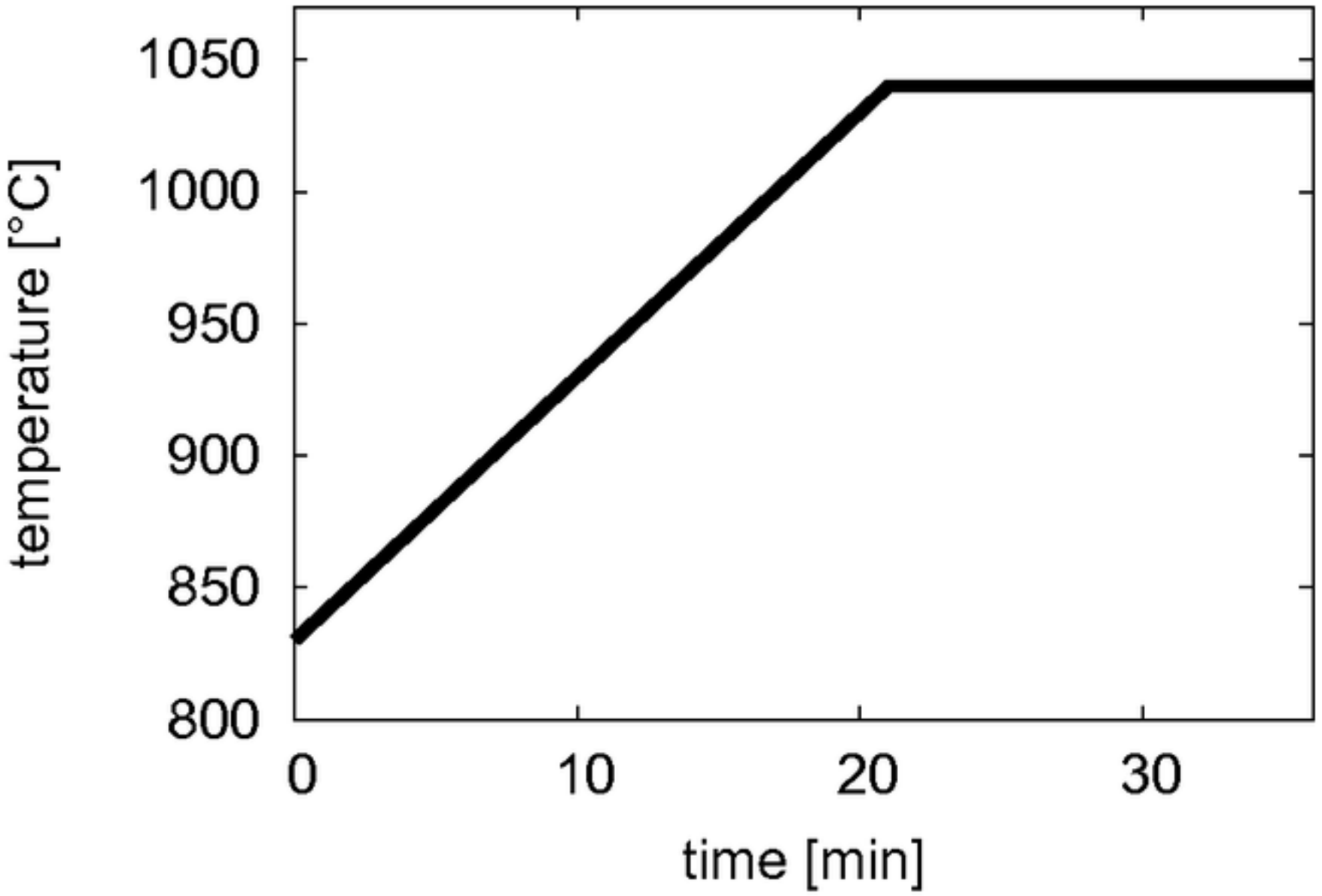

Figure 8b
Click here to download high resolution image

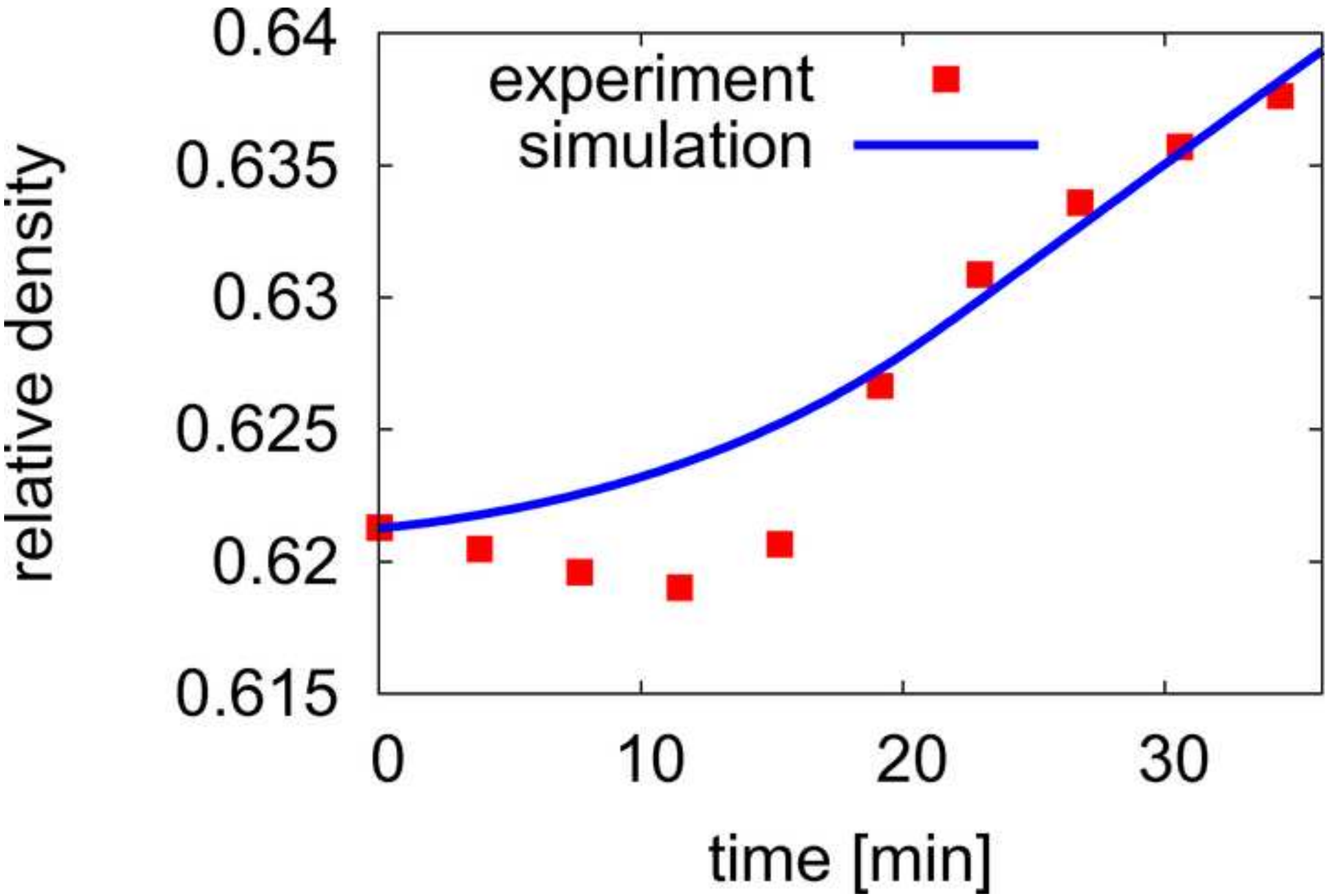

Figure 9a
Click here to download high resolution image

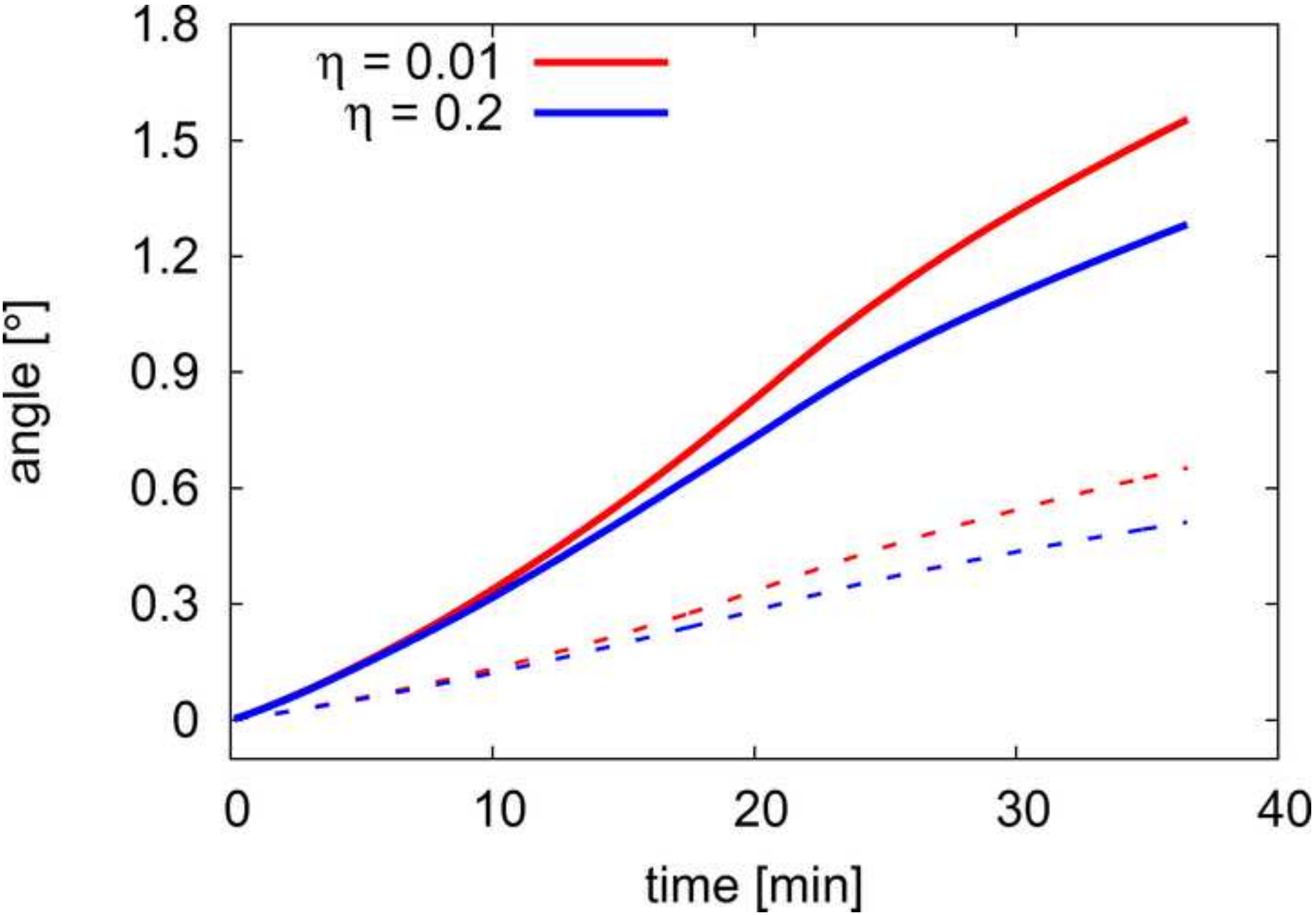

Figure 9b
Click here to download high resolution image

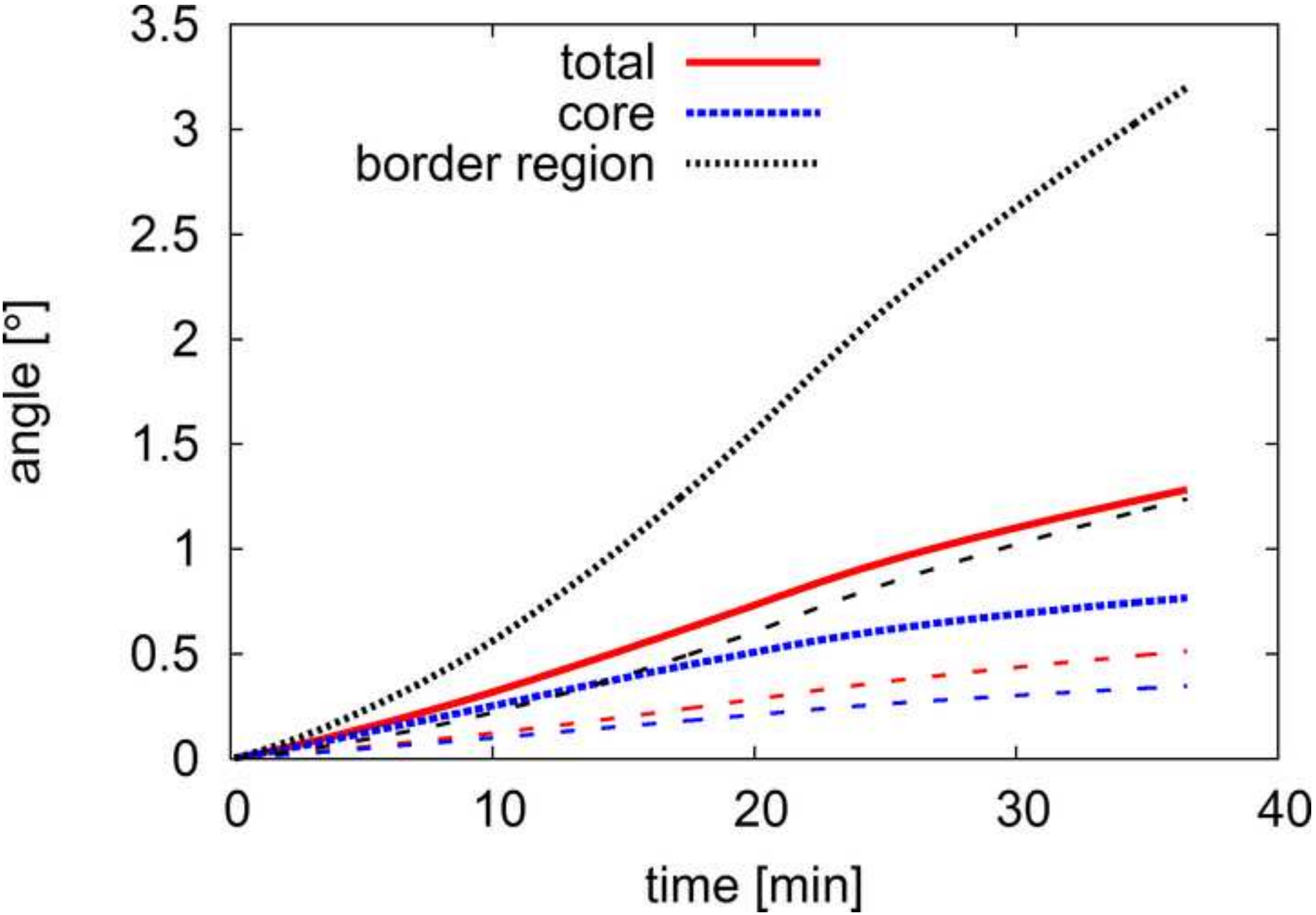

Figure 10
Click here to download high resolution image